Applied Physics A (2018) 124:633
https://doi.org/10.1007/s00339-018-2032-4

Applied Physics A
Materials Science & Processing

RAPID COMMUNICATION

Optoelectronic performance enhancement in pulsed laser deposited gallium-doped zinc oxide (GZO) films after UV laser crystallization

Qiong Nian[1] · David Look[2] · Kevin Leedy[3] · Gary J. Cheng[1]

Received: 12 June 2018 / Accepted: 11 August 2018 / Published online: 22 August 2018

Abstract

This study investigates the process–microstructure–property relationship during a UV laser crystallization of a transparent conductive layer—gallium doped zinc oxide (GZO) films after pulsed laser deposition (PLD). UV laser induced crystallization technique is able to apply ultra-fast post-treatment to modify GZO films with better structural and optoelectronics properties, suggesting a potential for large-scale manufacturing. A physical simulation model coupled laser–matter interaction and heat-transfer was utilized to study pulse laser heating and heat dissipation process. The laser crystallized GZO film exhibits low resistivity of $\sim 3.2 \times 10^{-4}$ Ω cm, high-Hall mobility of 22 cm^2/V s, and low sheet resistance of 22 Ω/sq. High-transmittance (T) over 90% at 550 nm is obtained (with glass substrate). The optoelectronic performance improved mainly attributes to grain boundary modification in the polycrystalline film, e.g., decrease of grain boundary density and passivation of electron trap at grain boundaries.

1 Introduction

Transparent conducting oxide (TCO) films, achieving both electrical conduction and optical transparency, are critical in many large consumer optoelectronic devices such as flat panel displays, photovoltaic cells, light emitting diodes, and electrochromic windows. Generally, these major applications require TCO exhibiting electrical resistivity less than 10^{-3} Ω cm while transparency more than 80% in visible (Vis) and near-infrared region (NIR) [1]. Until recently, over 90% mainstream market of TCOs were dominated by indium tin oxide (ITO), whose resistivity is approaching 10^{-4} Ω cm. However, due to the toxicity, scarcity and escalating cost of indium, there are urgent needs to seek alternative TCO films [1, 2].

Zinc oxides (ZnO) have drawn considerable attention for three decades as a promising substitute for ITO, since it is non-toxic, abundant and inexpensive, and has been demonstrated in many applications [3–7]. As an II–VI wide band gap (3.34 eV) semiconductor, ZnO exhibits high-Vis and NIR transparency [8]. However, pure ZnO has high-resistivity, which could be decreased by controllable n-type doping with group III elements. And un-doped ZnO thin films also show instable electrical properties, resulting from the chemisorption of oxygen at the surface and grain boundaries, which leads to higher resistivity [9]. The properties of the films can be stabilized by extrinsic dopants. Among n-type dopant group III elements, aluminum (Al) and gallium (Ga) were the most widely used. Ga dopant attracts more attention due to Ga–O has similar ionic (0.62 vs. 0.74 A) and covalent radii (1.26 vs. 1.25 A) as compared to Zn–O, meaning a highly Ga doped ZnO could be achieved without substantial lattice deformation.

Ga doped ZnO (GZO) is currently under intense investigation and development to replace ITO as the transparent conductive coating. To manufacture the GZO film, usually physical vapor depositions (PVD) was utilized to pursue high-electron conductivity [10–13]. Various deposition techniques are applied to prepare GZO films, such as sputtering [12], ion beam assisted deposition (IBAD) [11], atomic layer deposition (ALD) [13] and pulsed laser deposition (PLD) [10, 14], mainly operating at elevated temperatures. On the other hand, there are some reports of depositing GZO by low temperature PVD for optical devices or solution

✉ Gary J. Cheng
gjcheng@purdue.edu

[1] Birck Nanotechnology Center and School of Industrial Engineering, Purdue University, West Lafayette, IN 47906, USA

[2] Semiconductor Research Center, Wright State University, Dayton, OH 45435, USA

[3] Air Force Research Laboratory, Wright-Patterson AFB, Dayton, OH 45433, USA

based sol–gel fabrication, but poor optoelectronic properties were obtained [15, 16]. To the author's knowledge, the electrical conductivity of GZO film was difficult to exceed 4×10^{-4} Ω m, especially for low thickness (< 200 nm) film with high-optical transparency. To compete with ultra-conductive ITO film (conductivity approaching 1×10^{-4} Ω m), there is a need to develop a post-processing method to improve the electrical conductivity of GZO films deposited.

In this study, the UV laser crystallization post-treatment following deposition of GZO was explored to overcome the bottleneck. The GZO polycrystalline film was deposited by PLD onto the glass and followed by UV laser crystallization to minimize the extended defects and improve the optoelectronic performance as shown in Fig. 1. Significantly, the electrical conductivity of PLD deposited GZO film has been boosted up to around 1.5 times after post-UV laser processing. The conductivity achieved here is among the highest of all GZO transparent conductors film thickness in nanometers range. In addition, the process mechanism and process–microstructure relationship during UV laser crystallization in GZO thin film need systematic investigation. Herein, these key issues are tackled with experimental and modeling efforts, which could not only be applied to GZO film, but also provides guidance for deposition of other transparent conductive oxide layers on various substrates.

2 Experiment

The fabrication process consists of pulsed laser deposition (PLD) of GZO thin film and UV pulsed laser crystallization. Before PLD, a 50.4 mm diameter, 0.33 mm thick, (0001) orientation sapphire substrate was cleaned by acetone, methanol, and DI water in an ultrasonic cleaner for 5 min each, sequentially. The sapphire substrate was put into a high-vacuum chamber with a base pressure of 4.0×10^{-6} Torr. In this chamber ZnO (99.99%) and 2% Ga_2O_3-doped zinc oxide (GZO) targets with 50 mm diameters were ablated by a KrF excimer laser (λ of 248 nm with τ of 25 ns). The target-substrate distance was fixed at 80 mm. Targets and substrates rotated at 7 and 5 rpm, respectively. A 50 nm thick i-ZnO film was deposited on the sapphire substrate at laser fluence of 1.5 J/cm^2, repetition rate (RR) of 10 Hz for 20 min, and then 200 nm thick GZO was deposited at laser fluence of 0.5 J/cm^2, RR of 5 Hz for 90 min. Finally, a 250 nm thick GZO film was deposited at laser fluence of 0.5 J/cm^2, RR of 5 Hz for 90 min. O_2 pressure was set to be 150 and 1 mTorr for intrinsic zinc oxide (i-ZnO) and GZO films, respectively.

After PLD, the sample was transferred into a 10 mTorr vacuum chamber for the UV laser crystallization process. The same excimer laser was used with RR of 10 Hz. The laser beam was shaped to a square, top-hat profile (8 × 8 mm). The sample was placed on a motorized stage which enables translations along both *x*- and *Yy*-axes as shown in Fig. 1. Laser intensities used in the crystallization experiments ranged from 90 to 130 mJ/cm^2. The laser pulse number (*N*) used ranged from 10 to 200. After the laser crystallization, field emission scanning electron microscopy (FE-SEM) was used to measure the thickness of the GZO film via cross-section; top FE-SEM imaging was used to observe the surface structure. X-ray diffraction (XRD) was used to determine the GZO film's crystallinity and internal stress. Electrical resistivity and carrier mobility and concentration were measured by the Hall effect with the Van der Pauw method. Optical transmittance

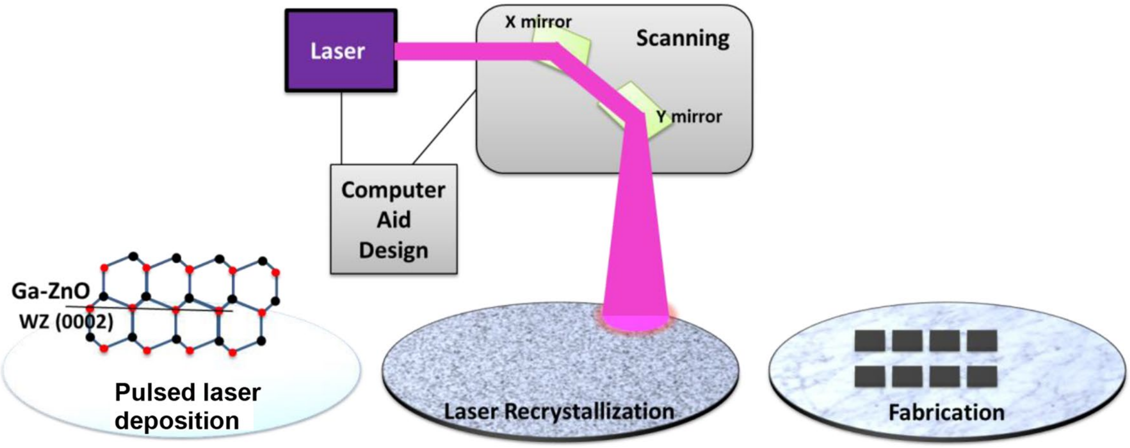

Fig. 1 Experiment set up: PLD was used to deposit GZO film onto glass substrate and a pulsed UV laser was scanning on the GZO film with enabled translations along both *x*- and *y*-axis to boost the process efficiency. Laser generation, intensity, scanning path and beam size could be integrated into computer aided design program for potential digital manufacturing. After laser crystallization, the treated film could be characterized

spectra were measured by Lambda 950 ultraviolet–visible and infrared spectrophotometers.

3 Results and discussion

Figure 1 depicts the setup of the experiment. As shown, pulsed laser deposition was used to coat wurtzite structure zinc oxide film onto glass substrate, with gallium dopant integrated in one source. After deposition of GZO by PLD, a pulsed UV laser was scanning on the GZO film with shaped square beam and top-hat profile with size of 8 × 8 mm and enabled translations along both *x*- and *y*-axis to boost the process efficiency. As shown, the laser generation, intensity, scanning path and beam size were integrated into computer aided design program for potential digital manufacturing. After UV laser crystallization, the treated film was characterized for quality analysis, device fabrication and practical application. During laser scanning, each laser pulse was able to introduce a localized high-temperature field from photo energy absorption, because the band gap of GZO film (~ 3.6 eV) is lower than the photo energy of excimer laser [17–19] (5 eV). This laser pulse induced heat treatment would lead to microstructure change and physical property improvement afterwards, which will be discussed later in this letter.

To understand the laser heating process, COMSOL Multiphysics® was applied to simulate the laser energy absorption [20–22] as schemed in Fig. 2a. The electromagnetic module (EM) was used to simulate laser irradiation, and the heat transfer module (HT) was used to describe the temperature increase in GZO polycrystalline film during a single laser pulse delivery. Laser beam is assumed to be in the fundamental mode with wavelength of 248 nm for crystallization process. Primary controlling parameters are laser pulse energy (E), pulse duration (τ), and beam radius (γ). The spatial distribution of laser pulse could be written as Eq. (1).

$$E = E_o \times \exp\left[-2\left(\frac{x^2}{r^2} + \frac{y^2}{r^2}\right)\right]. \tag{1}$$

In this equation, E_o represents the central pulsed energy of laser beam, and x, y are coordinates. Temporal distribution of the laser is represented by normalized Weibull function which could manipulate the pulse duration and power by modifying its shape factors. The incident laser heating was induced by near-field scattering occurring on polycrystalline GZO structure, which can be depicted by resistive heating (Q_{RH}), and expressed in Eq. (2)

$$Q_{RH} = \frac{1}{2}\,\mathrm{Re}\,\{\sigma E E^* - j\omega E D^*\}. \tag{2}$$

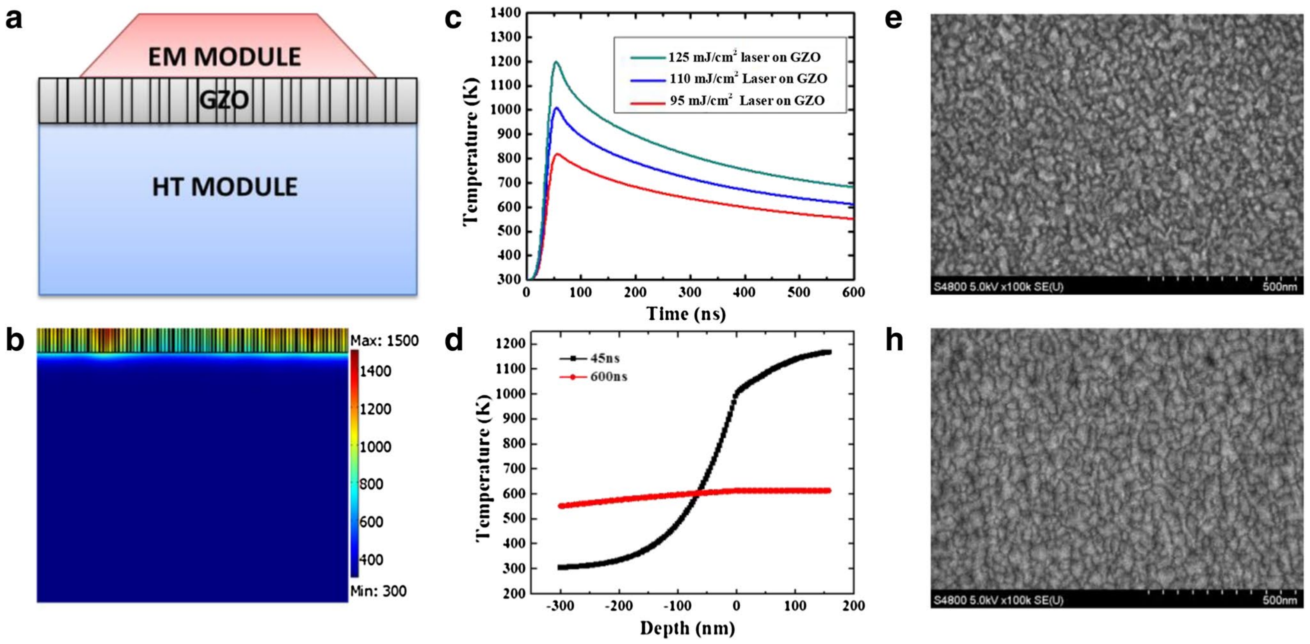

Fig. 2 **a** Comsol multiphysics simulation set up, with EM module to simulate laser–mater interaction and HT module to simulate heat transfer occurs in GZO film and substrate. **b** Laser selective heating occurs at 45 ns simulation time, in which thermal energy was mainly absorbed by GZO film rather than glass substrate due to high-absorption coefficient. **c** Temperature evolution of GZO film top surface during laser crystallization with single pulse delivery. **d** Temperature distribution along depth (160 nm GZO film to − 300 nm substrate) at simulation time of 45 and 600 ns for single pulse delivery. **e** SEM surface morphology of as-deposited GZO film. **f** SEM surface morphology of laser crystallized GZO film

The governing equations in the EM module in this study are Ampere's law with Maxwell's correction and Faraday's law of induction as shown in Eq. (3). Due to the conservation of energy for the electromagnetic filed, where the first term and second term on left hand side represent the resistive losses and radiative losses, respectively.

$$\int J \times E \mathrm{d}V + \oint (E \times H) \times n \mathrm{d}s = -\oint \left(E \frac{\partial D}{\partial t} + H \frac{\partial B}{\partial t} \right) \mathrm{d}V. \tag{3}$$

During resistive heating, as heat transfer occurs, temperature (T) would form in the system. A typical T field is given by solving a coupled HT module with Q_{RH} as the heating source. The heat transfer equation is governed by Eq. (4)

$$\begin{aligned} Q_{\mathrm{RH}} = {} & \rho(X,\ T)c_{\rho}(X,\ T)\frac{\partial T(X,t)}{\partial t} - \nabla[\kappa(X,T)\nabla T(X,T)] \\ & + \rho(X,T)c_{\rho}(X,\ T)v_{s}\nabla T(x,t). \end{aligned} \tag{4}$$

Equations (2)–(4) are then numerically solved in coupled EM module and HT module as shown in Fig. 2a. Laser parameters, materials properties and film properties are set as essential input in the simulation. As calculated in Fig. 2b, heat energy was mainly absorbed by the GZO layer due to higher absorption coefficient comparing to glass substrate. Figure 2b represents the temperature distribution at the simulation time of 45 ns, in which heat transfer into bottom glass substrate is still insufficient. The highest temperature in GZO film reaches 1500 K (on some hot spots as show in Fig. 2b), while low temperature less than 600 K was observed in substrate. However, heat transfer occurs then due to temperature gradient in the GZO-substrate interface. The result of one laser pulse irradiation and afterwards are represented in Fig. 2c, the average temperature of GZO film increases to 800–1200 K in 45 ns depending on laser intensity of 90–125 mJ/cm, respectively. Then the temperature of the GZO would be lowered by thermal dissipation, as demonstrated at 600 ns simulation time, before subsequent laser pulse delivery. This fast heating and following thermal dissipation also could be demonstrated by Fig. 2d, in which the temperature distribution over GZO film–substrate interface was recorded. In simulation time of 45 ns (black curve), thermal energy exchange from laser beam to GZO film governs. GZO film located from depth of 0–160 nm shows apparent elevated temperature (1000–1200 K). However, when depth goes from 0 to − 300 nm for substrate, a sharp decrease to room temperature (300 K) was observed. This discontinuous circumstance renders the fact of laser induced selective heating. On the other side, thermal dissipation is able to transfer heat into substrate across interface drive by high-temperature gradient. This is also demonstrated by simulation result in 600 ns (red curve), in which both GZO film and substrate swing around 600 K. This fast thermal dissipation indicates a fast cooling process of GZO film after initial selective laser heating. Thereby multiple laser pulse shinning with repeatable heating–cooling process is able to drive microstructure change of target film, similarly to abnormal grain growth in solid recrystallization process [20, 22]. Figure 2e, f shows the top view FESEM image of the laser scanned film comparing to as deposited film, as thermal energy continues along multi laser pulse delivery (200 pulses in this image), the polycrystalline microstructure tends to reform large grains and faceted boundaries. Comparing untreated (e) to treated (f), it is found that the crystallized film is more compact and continuous, implying the crystallinity of the GZO film has been significant enhanced [18, 23].

The changes of grain morphology and surface roughness after laser crystallization were revealed by atomic force microscope (AFM), as shown in Fig. 3. Note that the standard deviation on the roughness values (Ra, arithmetical mean deviation of the assessed profile) are 0.21 nm, 0.18 nm, 0.14 nm, 0.16 nm for 105.6 mJ/cm^2 after 1p, 10p, 50p, 200p, respectively and 0.41 nm, 0.39 nm, 0.40 nm, 0.32 nm, respectively, for 113.7 mJ/cm^2 after 1p, 10p, 50p, 200p, respectively. The grain structure before laser crystallization was shown as nanoparticles stacked together after PLD (Fig. 3a, d). After laser crystallization under laser fluence of 105.6 mJ/cm^2, the grain boundary between the nanoparticles are much better connected with each other. With the laser pulse number (p) increases from 10p to 50p and 200p, the grain structure become denser. The roughness reduces significantly from 1.45–0.914 nm after 50p, which contribute to less optical scattering of the thin film. As laser fluence increases to 113.7 mJ/cm^2, the grain size increases more significantly than under 105.6 mJ/cm^2. Clear grain boundary can be seen after laser crystallization with 50p and 200p.

The crystallinity modification of GZO film could be verified by X-ray diffraction patterns (XRD) as shown in Fig. 4a. Typical peak located at $2\theta = 34.6°$ is well indexed to wurtzite zinc oxide crystal planes of (002). Comparing to signals before laser crystallization, it is clear seen that (002) peak of GZO film achieve much higher intensity after multiple laser pulse delivery (200 pulses), implying textured crystal orientation. Further exploring of the structural modification on GZO film was characterized by calculating the full width half maximum (FWHM) and the grain size according to XRD peaks. The FWHM was measured by the Lorenz fit of the (002) peak, while crystal size could be drawn from Bragg's equation with FWHM as the input [24, 25]. Figure 4b illustrates the FWHM and grain size of the GZO film as a function of laser processing conditions. Apparently with multiple laser pulse delivery for both laser intensity of 105.6 and 113.7 mJ/cm^2, the FWHM show much narrower FWHM and grain show much larger size comparing to as-deposited

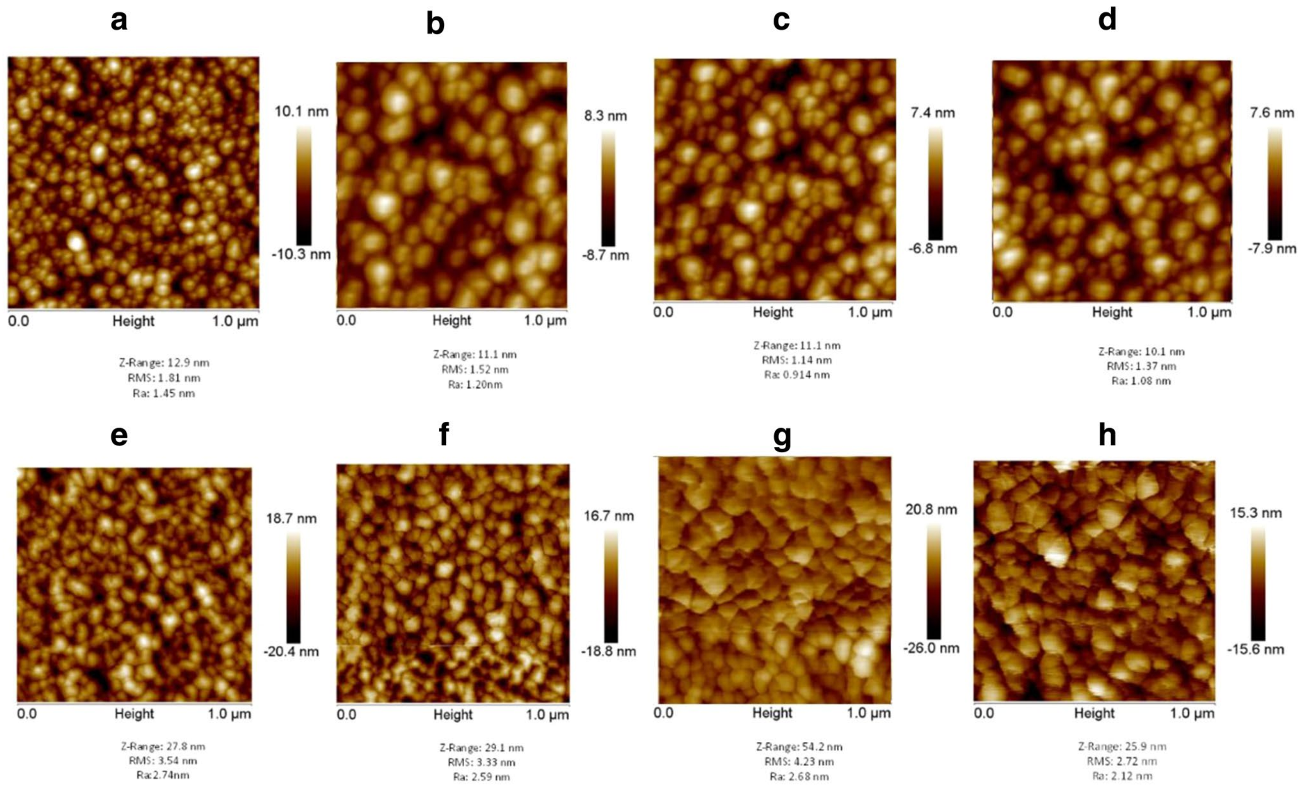

Fig. 3 AFM images and roughness of **a** starting film after PLD; **b–d** after **a** and laser crystallization under 105.6 mJ/cm^2, 10p, 50p, 200p, respectively, **e** starting film after PLD; **f–h** after **a** and laser crystallization under 113.7 mJ/cm^2, 10p, 50p, 200p, respectively

film. These results are in good agreement with Fig. 3, in which large grain and faceted boundaries are formed combining with homogeneous and continuous surface [18, 26].

To study the effects of crystallization on GZO film electrical performance, Hall measurement was carried out. With small size grain merged and larger size grain formed, it is straightforward to draw that grain boundary density was decreased. Furthermore, since the grain shape changed to facetted and surface compacted, the inter grain defects like voids, gaps and discontinuity decrease, which originally may create energy levels in the band gap that tend to trap the free electrons and decrease their lifetime [27]. Both lower grain boundary density and less electron traps at boundaries are able to diminish the grain boundary barrier scattering and boost the electron mobility cross boundaries, which contribute to or dominate the polycrystalline GZO film mobility [9, 28, 29]. As demonstrated in Fig. 4c, d, the electrical properties of GZO films as a function of laser parameters, detected by Hall effect measurement was plotted. After the crystallization, a strong increase in mobility and decrease in sheet resistance are observed for all different laser parameters as shown in Fig. 4c, d. The as deposited GZO film performs a Hall mobility of 16 cm^2/V s, on contrast, the Hall mobility increases to ~ 20.2 ± 0.20 cm^2/V s with 10 laser pulses delivery and ~ 21.9 ± 0.38 cm^2/V s with 200 laser pulses delivery. Note that, the improvement indicates an around 20% increase of electron mobility after UV laser processing, which is critical for many applications in optoelectronic industry to relax the tradeoff between optical transparency and electrical conductivity of GZO thin film.

To delve into the mechanism of electron mobility improvement, the electron's mean free path l could be calculated using the following Eq. (5) [24, 25]

$$l = \frac{h}{2e}\left(\frac{3N}{\pi}\right)^{\frac{1}{3}}\mu, \tag{5}$$

where h is the Plank's constant, e is the electron charge, N is the carrier concentration and μ is the Hall mobility. Inputting Hall measurement values in Table 1, the mean free path of the carriers for as-deposited GZO film could be calculated as 3.1 nm, which is in the same range of grain size shown in Fig. 4b. This indicates the electron mobility inside polycrystalline GZO film is mainly dominated by grain boundary scattering mechanism. To analyze the grain boundary scattering dominated mobility μ_g enhancement of GZO film after laser crystallization, the polycrystalline structure and energy

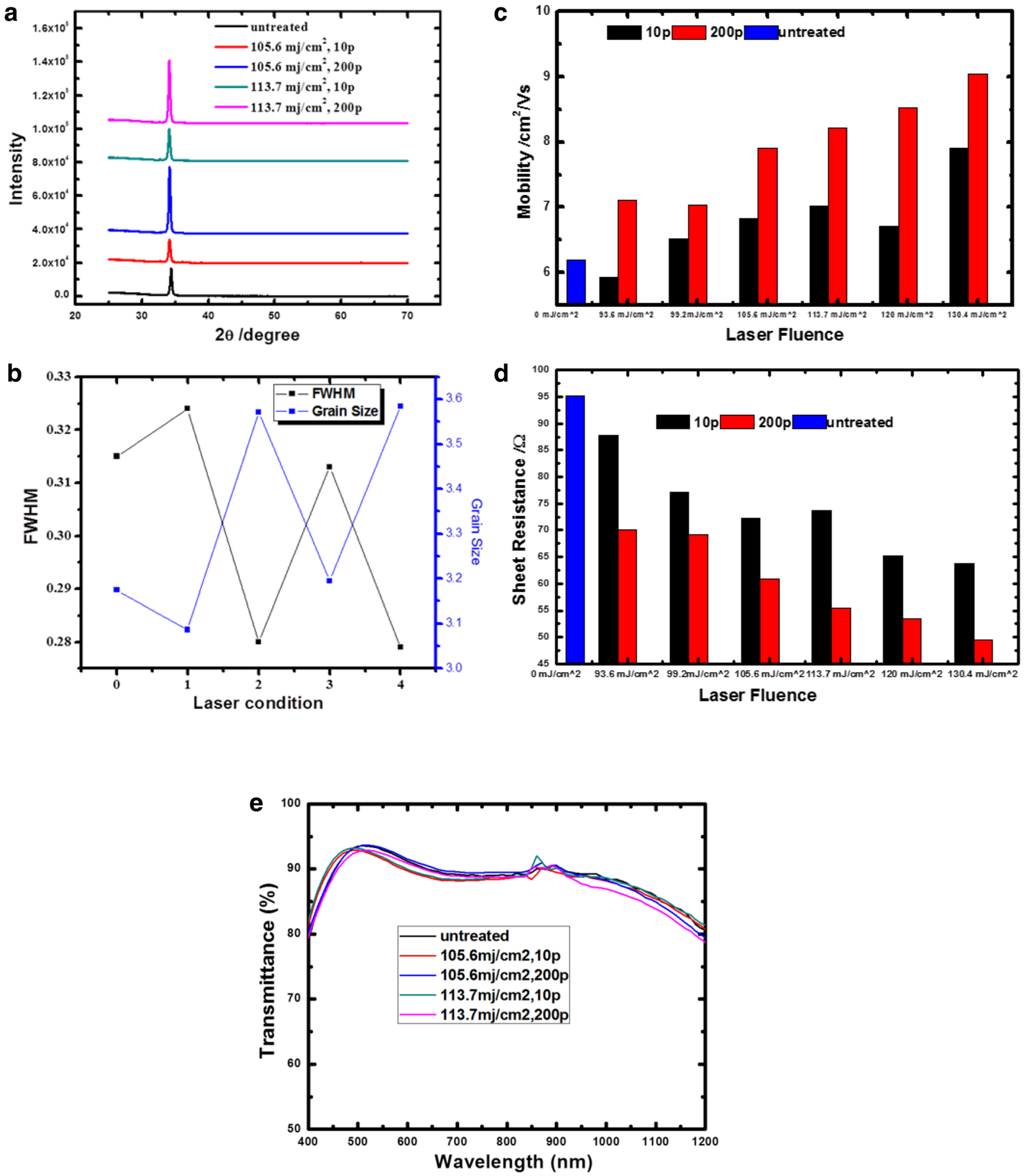

Fig. 4 **a** θ–2θ XRD patterns of GZO films as-deposited by PLD and processed by laser at 105.6 mJ/cm^2, 113.7 mJ/cm^2 with 10 pulses and 200 pulses, respectively. The GZO films have a preferred (002) out-of-plane orientation on substrate. **b** Corresponding FWHM and grain size characterization of GZO films as-deposited and processed by post-laser crystallization. **c** Laser parameter dependence of Hall measurements collected electron mobility. **d** Laser parameter dependence of Hall measurements collected sheet resistance

Table 1 Laser crystallization conditions on GZO films and the derived Hall measurement performance

Laser intensity (mJ/cm^2)	Pulses	R_{sheet} (Ω/sq)	ρ (Ω cm)	μ (cm^2/V s)	N_{eff} (cm^3)
0	0p	33.23	5.12×10^{-4}	16.1	-7.56×10^{20}
105.6	10p	26.98	4.05×10^{-4}	20.1	-7.66×10^{20}
105.6	200p	21.95	3.29×10^{-4}	21.8	-8.70×10^{20}
113.7	10p	27.18	4.08×10^{-4}	20.5	-7.46×10^{20}
113.7	200p	21.59	3.24×10^{-4}	22.1	-8.73×10^{20}

level could be referred [20]. The grain boundary density is determined by grain size L while the scattering intensity at grain boundaries is determined by energy potential barrier height Φ_b. The latter one is controlled by electron trap density (N_t) and the free electron concentration (N_{eff}). Seto [30] and Baccarani et al. [31] extend Petriz model [32] on the basis of the first approximation to describe the energy potential barrier at grain boundary as shown in Eq. (6) [9, 28, 29, 33], in which $\varepsilon\epsilon_0$ is the static dielectric constant, m^* is the electron effective mass and e is the elementary charge.

$$\mu_g = \mu_0 \exp\left(-\frac{\Phi_B}{kT}\right) = \frac{eL}{\sqrt{2\pi m^* kT}} \exp\left(-\frac{e^2 N_t^2}{8kT\varepsilon \int_0 N_{\text{eff}}}\right). \tag{6}$$

The basic result of this equation is based on electrons transport through grain boundary by thermionic emission over the barrier, taking into account of electron traps as a depletion region formed on either side of the grain boundary barrier. Based on Eq. (6), the electron mobility inside GZO film is mainly dominated by grain size L and electro trap density at grain boundaries N_t. Thereby, after laser crystallization, the increased mobility by Hall measurement could be used for reverse derivation. As derived with inputting of Hall mobility of ~ 20 and ~ 22 cm^2/V s into Eq. (5), the mean free path of electrons should be 3.8 and 4.2 nm, respectively. This value is slightly higher comparing to the measured grain size in Fig. 4b (3.2 and 3.6 nm), implying the larger grain formation is the main reason for electron mobility increase. However, there might be other possible reason such as decrease of electron trap density N_t contributing to electron mobility enhancement in GZO film after laser crystallization. The decrease of electron trap density attributes to both removal of extended defects (mid-band energy level) and desorption of oxygen species at grain boundaries [17, 28]. Desorption of oxygen species by UV laser exposure would release free carriers from traps which is stated by prior reports [17, 28]. Subject to current series of samples, this could be demonstrated by a moderate increase of carrier concentration after laser as shown in Table 1.

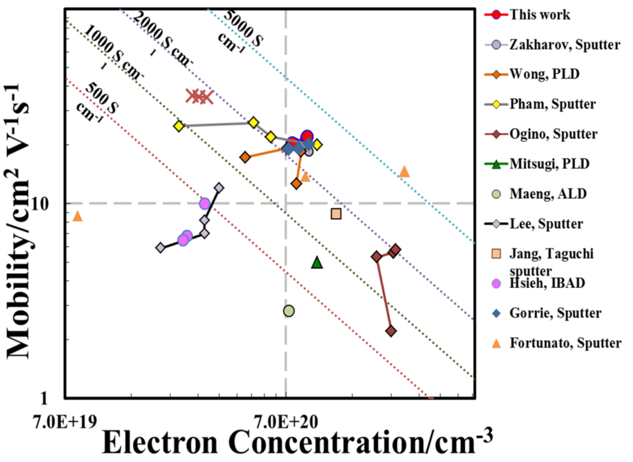

Fig. 5 **a** Influence of laser crystallization on transmittance: visible–IR transmittance spectrum (with glass substrate during measuring) processed GZO films encounter a blue shift. **b** Electron mobility vs. electron concentration for GZO films in this work comparing with high-vacuum deposition by 12 research groups. The red spots show current work, the other marked points and curves represent high-mobility GZO films listed for comparison. The diagonal dashed lines show constant conductivity on a log–log scale

The electron mobility increase would result in sheet resistance decreases from 33 to 21 Ω/sq, when multiple laser pulses were delivered to GZO film with optimal laser intensity. As demonstrated in Fig. 4d, the sheet resistance of GZO films varies as a function of laser parameter. Both higher laser intensity and multiple laser pulses would contribute to low sheet resistance. The optimal laser intensity and pulse number was observed as 113.7 mJ/cm^2 and 200 pulses. The optimal laser conditions could be varied according to different metal oxide and different substrate, however, are straightforward to discover with a series of experiments. And note that, although conductivity enhancement associates with a strong increase in carrier mobility, a moderate increase in carrier concentration also should not be neglected. This moderate increase of carrier concentration inside GZO film not only reflects in sheet resistance decrease, but also in optical transmittance change. As demonstrated in Fig. 4e, the optical transmittance as a function of wavelength, it is clearly that the optical transmittance encounters a slight blue shift after laser crystallization. The relatively decreased transmittance in near-infrared range (700–1200 nm) indicates free carrier absorption, which is in good agreement with moderate carrier concentration increase in Table 1. Note that, the transmittance of current series of samples were all measured with glass substrate, which still achieve around 90% transmittance in visible range.

The high-optical transparency and simultaneous low sheet resistance of the laser crystallized GZO film imply a significantly improved overall optoelectronic property, which could also be demonstrated in Fig. 5. Figure 5 shows electron mobility vs. free electron concentration data for GZO thin films deposited by several high-vacuum methods from 12 groups [10–13, 34–41]. These prior advancements have achieved highest electrical conductivity on different substrates (polymer, glass and sapphire), which provide a comparison with our results based on laser crystallization (red spots in Fig. 5). Comparing PLD and followed laser crystallization method in our work with other groups in Fig. 5, the laser crystallized GZO films exhibit high-mobility (22 cm^2/V s), implying diminishing grain boundary barrier and decreasing grain boundary density. The highest electrical conductivity of current series of sample achieves over 3000 S/cm, which performs better than almost all the prior vacuum methods, as stated in Fig. 5. Additionally, grain boundary density also could be affected by film thickness and crystal growth method which would further influence the carrier mobility [20, 25]. And according to Eq. (6), the grain boundary density influences the grain boundary mobility with a linear factor. This supplies an explanation that charge mobility in our study is still lower than some high-vacuum fabrications. However, considering the 160 nm thick top layer in our work is thinner than prior advancements, our laser crystallization has potential to achieve even higher carrier mobility.

4 Conclusion

In summary, the method of PLD followed by laser crystallization was explored to deposit transparent conductive GZO films onto glass substrate. This UV laser induced crystallization technique is able to apply fast post-heat treatment to modify the microstructures in GZO films with better optoelectronics properties, suggesting a potential for large-scale manufacturing. Multiphysics simulation model coupled laser–matter interaction and heat transfer was utilized to study pulse laser heating and heat dissipation process. The laser crystallized GZO film exhibits low resistivity of $\sim 3.2 \times 10^{-4}\ \Omega$ cm, high-Hall mobility of 22 cm^2/V s, and low sheet resistance of 22 Ω/sq. The high-transmittance (T) over 90% at 550 nm is obtained for sample with glass substrate. The optoelectronic performance improved mainly attributes to the polycrystalline film grain boundary modification by UV laser such as grain boundary density decrease and the passivation of electron traps near grain boundary, as demonstrated by the results from material characterization. The ultra-fast and flexible laser treatments have the potential to apply in semiconductor oxides layers after deposition of thin film by physical vapor deposition, sol–gel, ink-jet printing, or spray-coating.

Acknowledgements The authors acknowledge the funding support from US National Research Council, and Air Force Research Laboratory.

References

1. T. Minami, MRS Bull. **25**(08), 38 (2000)
2. K. Ellmer, Nat Photonics **6**(12), 809 (2012)
3. C.F. Tan, A.K.S.S. Zin, Z. Chen, C.H. Liow, H.T. Phan, H.R. Tan, Q.-H. Xu, G.W. Ho. ACS Nano **12**(5), 4512 (2018)
4. K. Xu, J. Wu, C.F. Tan, G.W. Ho, A. Wei, M. Hong, Nanoscale **9**(32), 11574 (2017)
5. I. Kapilevich, A. Skumanich, in *Presented at the Photovoltaic Specialists Conference (PVSC), 2009 34th IEEE*, 2009 **(unpublished)**
6. B. O'Neill, *Presented at the Photovoltaic Specialists Conference (PVSC), 2010 35th IEEE*, 2010 **(unpublished)**
7. T.J. Coutts, T.O. Mason, D.S. Ginley, Proc. Electrochem. Soc. **99**, 274 (1999)
8. R.G. Gordon, MRS Bull. **25**(08), 52 (2000)
9. K. Ellmer, in *Transparent Conductive Zinc Oxide*, vol. 104, ed. by K. Ellmer, A. Klein, B. Rech (Springer, Berlin, 2008), p. 35
10. L.M. Wong, S.Y. Chiam, J.Q. Huang, S.J. Wang, W.K. Chim, J.S. Pan, Sol. Energy Mater. Sol. Cells **95**(8), 2400 (2011)
11. J.H. Hsieh, C.K. Chang, H.H. Hsieh, Y.J. Cho, J. Lin, Vacuum **118**, 43 (2015)
12. X.-L. Chen, F. Wang, X.H. Geng, Q. Huang, Y. Zhao, X.-D. Zhang, Thin Solid Films **542**, 343 (2013)
13. W.J. Maeng, J.-S. Park, J. Electroceram. **31**(3), 338 (2013)
14. K. Xu, C. Zhang, R. Zhou, R. Ji, M. Hong, Opt. Express **24**(10), 10352 (2016)
15. S. Chen, M.E.A. Warwick, R. Binions, Sol. Energy Mater. Sol. Cells **137**, 202 (2015)
16. K. Nayak Pradipta, Y. Jihoon, K. Jinwoo, C. Seungjun, J. Jaewook, L. Changhee, H. Yongtaek, J. Phys. D Appl. Phys. **42**(3), 035102 (2009)
17. H. Hagendorfer, K. Lienau, S. Nishiwaki, C.M. Fella, L. Kranz, A.R. Uhl, D. Jaeger, L. Luo, C. Gretener, S. Buecheler, Y.E. Romanyuk, A.N. Tiwari, Adv. Mater. **26**(4), 632 (2014)
18. M.Y. Zhang, Q. Nian, G.J. Cheng, Appl. Phys. Lett. **100**(15), 151902 (2012)
19. M.Y. Zhang, Q. Nian, Y. Shin, G.J. Cheng, J. Appl. Phys. **113**(19), 193506 (2013)
20. Q. Nian, M. Callahan, M. Saei, D. Look, H. Efstathiadis, J. Bailey, G.J. Cheng, Sci. Rep. **5**, 15517 (2015)
21. Q. Nian, M. Callahan, D. Look, H. Efstathiadis, J. Bailey, G.J. Cheng, APL Mater. **3**(6), 062803 (2015)
22. Q. Nian, M.Y. Zhang, Y. Wang, S.R. Das, V.S. Bhat, F. Huang, G.J. Cheng, Appl. Phys. Lett. **105**(11), 111909 (2014)
23. Z. Zhang, C. Bao, S. Ma, S. Hou, Appl. Surf. Sci. **257**(17), 7893 (2011)
24. J.-Y. Tseng, Y.-T. Chen, M.-Y. Yang, C.-Y. Wang, P.-C. Li, W.-C. Yu, Y.-F. Hsu, S.-F. Wang, Thin Solid Films **517**(23), 6310 (2009)
25. T. Yamada, H. Makino, N. Yamamoto, T. Yamamoto, J. Appl. Phys. **107**(12), 123534 (2010)
26. M.Y. Zhang, G.J. Cheng, Appl. Phys. Lett. **99**(5), 051904 (2011)
27. D.C. Look, C. Coşkun, B. Claflin, G.C. Farlow, Physica B Condens. Matter **340–342**(0), 32 (2003)
28. L. Ding, S. Nicolay, J. Steinhauser, U. Kroll, C. Ballif, Adv. Funct. Mater. **23**(41), 5177 (2013)
29. E. Alan, Delahoy, S. Guo, in *Handbook of Photovoltaic Science and Engineering* (Wiley, Hoboken, 2011), pp. 716
30. J.Y.W. Seto, J. Appl. Phys. **46**(12), 5247 (1975)
31. G. Baccarani, B. Riccò, G. Spadini, J. Appl. Phys. **49**(11), 5565 (1978)

32. R.L. Petritz, Phys. Rev. **104**(6), 1508 (1956)
33. J.G. Lu, Z.Z. Ye, Y.J. Zeng, L.P. Zhu, L. Wang, J. Yuan, B.H. Zhao, Q.L. Liang, J. Appl. Phys. **100**(7), 073714 (2006)
34. D.P. Pham, H.T. Nguyen, B.T. Phan, V.D. Hoang, S. Maenosono, C.V. Tran, Thin Solid Films **583**, 201 (2015)
35. T. Ogino, J.R. Williams, K. Watanabe, I. Sakaguchi, S. Hishita, H. Haneda, Y. Adachi, T. Ohgaki, N. Ohashi, Thin Solid Films **552**, 56 (2014)
36. F. Mitsugi, N. Umeda, N. Sakai, T. Ikegami, Thin Solid Films **518**(22), 6334 (2010)
37. S.E. Park, J.C. Lee, P.K. Song, J.-H. Lee, J. Korean Phys. Soc. **54**(3), 1283 (2009)
38. C. Jang, Z. Ye, Q. Jiang, Mater. Sci. Semicond. Process. **30**, 152 (2015)
39. A.N. Zakharov, K.V. Oskomov, S.V. Rabotkin, A.A. Solov’ev, N.S. Sochugov, Tech. Phys. **55**(5), 719 (2010)
40. C.W. Gorrie, A.K. Sigdel, J.J. Berry, B.J. Reese, M.F.A.M. van Hest, P.H. van Hest, P.H. Holloway, D.S. Ginley, J.D. Perkins, Thin Solid Films **519**(1), 190 (2010)
41. E. Fortunato, L. Raniero, L. Silva, A. Gonçalves, A. Pimentel, P. Barquinha, H. Águas, L. Pereira, G. Gonçalves, I. Ferreira, E. Elangovan, R. Martins, Sol. Energy Mater. Sol. Cells **92**(12), 1605 (2008)